Polar Science xxx (xxxx) xxx

Contents lists available at ScienceDirect

Polar Science

journal homepage: www.elsevier.com/locate/polar

Methane release from open leads and new ice following an Arctic winter storm event

Anna Silyakova [a], Daiki Nomura [b,c,d,*], Marie Kotovitch [e,f], Agneta Fransson [g], Bruno Delille [e], Melissa Chierici [h], Mats A. Granskog [g]

[a] CAGE, Centre for Arctic Gas Hydrate, Environment and Climate, Department of Geosciences, UiT the Arctic University of Norway, Tromsø, Norway
[b] Field Science Center for Northern Biosphere, Hokkaido University, 3–1–1, Minato–cho, Hakodate, Hokkaido, 041–8611, Japan
[c] Faculty of Fisheries Sciences, Hokkaido University, 3–1–1, Minato–cho, Hakodate, Hokkaido, 041–8611, Japan
[d] Arctic Research Center, Hokkaido University, Kita–21, Nishi–11, Kita–ku, Sapporo, Hokkaido, 001–0021, Japan
[e] Unité d'océanographie chimique, Freshwater and Oceanic sCience Unit of ReSearch, Université de Liège, Belgium
[f] Laboratoire de Glaciologie, DGES, Université Libre de Bruxelles, Belgium
[g] Norwegian Polar Institute, Fram Centre, 9296, Tromsø, Norway
[h] Institute of Marine Research, Fram Centre, Tromsø, Norway

ARTICLE INFO

Keywords:
Methane
Arctic ocean
Sea ice
Wintertime
Storm

ABSTRACT

We examine an Arctic winter storm event, which led to ice break–up, the formation of open leads, and the subsequent freezing of these leads. The methane (CH_4) concentration in under–ice surface water before and during the storm event was 8–12 nmol L^{-1}, which resulted in a potential sea–to–air CH_4 flux ranging from +0.2 to +2.1 mg CH_4 m^{-2} d^{-1} in open leads. CH_4 ventilation between seawater and atmosphere occurred when both open water fraction and wind speed increased. Over the nine days after the storm, sea ice grew 27 cm thick. Initially, CH_4 concentrations in the sea ice brine were above the equilibrium with the atmosphere. As the ice grew thicker, most of the CH_4 was lost from upper layers of sea ice into the atmosphere, implying continued CH_4 evasion after the leads were ice–covered. This suggests that wintertime CH_4 emissions need to be better constrained.

1. Introduction

CH_4 emissions in a warming Arctic climate are suggested to increase gradually (Schuur et al., 2015). Arctic Ocean (AO) waters, which are largely covered by sea ice, receive CH_4 gas from numerous geological sources, such as dissociating gas hydrates (Paull et al., 2007; Westbrook et al., 2009), gas reservoirs (e.g., sub-sea and land-based hydrocarbon seeps) (Portnov et al., 2016; Platt et al., 2018), and decaying submarine permafrost (Portnov et al., 2013). Depending on the strength of geological plume and water depth, some of the CH_4 released at seafloor reaches the surface waters (Shakhova et al., 2010; Graves et al., 2015; Silyakova et al., 2020; Thornton et al., 2020). Surface AO waters are also known for biologically produced CH_4 excess due to nutrient limitation (Damm et al., 2010, 2015a) and because of physical rejection of brine containing CH_4 during sea ice growth and downward brine flushing with meltwater during sea ice melt (Damm et al., 2015b).

Different inputs result in an increase of CH_4 concentration in the water column. Increasing CH_4 concentration from deep to surface waters and surface water CH_4 super–saturation was found in ice–covered regions of the AO (e.g., Kvenvolden et al., 1993; Fenwick et al., 2017). While surface stratification hinders excess CH_4 from mixing with deeper waters (Damm et al., 2015b), sea ice, on the other hand, hampers direct and rapid CH_4 release to the atmosphere. Therefore, CH_4 accumulates and resides in under–ice surface waters for prolonged periods (Kitidis et al., 2010). As a result, a greater concentration of dissolved CH_4 in waters below the sea ice cover when compared to open waters is found in many regions of the AO (e.g., Kvenvolden et al., 1993; Kitidis et al., 2010; Shakhova et al., 2010; Shakhova et al., 2015; Damm et al., 2015b).

CH_4 accumulates beneath sea ice in the AO waters (Damm et al., 2018) before being oxidized by microbes (Damm et al., 2007, 2015a; Kitidis et al., 2010), which is the primary removal mechanism of CH_4 in ocean waters (Reeburgh, 2007), or released into the atmosphere through fractures in sea ice. The latter could potentially be a significant CH_4

* Corresponding author. Field Science Center for Northern Biosphere, Hokkaido University, 3–1–1, Minato–cho, Hakodate, Hokkaido, 041–8611, Japan.
E-mail address: daiki.nomura@fish.hokudai.ac.jp (D. Nomura).

https://doi.org/10.1016/j.polar.2022.100874
Received 4 April 2022; Received in revised form 18 July 2022; Accepted 19 July 2022
Available online 3 August 2022

source to the atmosphere in the Arctic (Kort et al., 2012). Climate change increases the mean speed and deformation of the Arctic sea ice, which results in an increasing amount of fractures in the ice pack (Rampal et al., 2009). Arctic storms contribute to fractures of summer multi–year sea ice (Asplin et al., 2014), and fracturing can also increase in the thinner and younger Arctic ice pack in winter (Itkin et al., 2017), which in turn increases the potential for winter air–sea gas exchange (Fransson et al., 2017). Further high wind speeds during storms promote the gas exchange processes at the air–sea interface in open water leads (Wanninkhof, 2014).

In this paper, we focus on CH_4 dynamics in under–ice water and new thin sea ice formed in open water leads during and after a major winter storm in February 2015 in the Nansen Basin of the AO. We report concentrations of dissolved CH_4 in under–ice surface water and post–storm formed thin sea ice; CH_4 temporal dynamics within sea ice over six days; and estimated the sea–to–air CH_4 flux from open water leads at the time of ice break up during the storm. This implies that wintertime fracturing of the otherwise rather impermeable ice pack can result in significant CH_4 fluxes that need to be better constrained to understand their role in the Arctic CH_4 budget.

2. Methods

2.1. N–ICE2015 campaign and the major storm event

The Norwegian research vessel (R/V) Lance froze into the Arctic ice pack in the Arctic Ocean's Atlantic sector in January 2015 to study the environmental processes until June same year as part of the Norwegian young ICE (N–ICE2015) campaign. The data used in this study was collected when R/V Lance was anchored to Floe 1 of N–ICE2015 from January 15 to February 21 when newly formed thin sea ice covered open leads after the major storm event (Fig. 1). The major N–ICE2015 storm event M2 started on February 3 and ended on February 8 (Cohen et al., 2017). This storm was specified as a winter storm (Itkin et al., 2018). Atmospheric pressure decreased by 14 hPa in 6 h, peak wind speed at 10 m height was 22 m s^{-1}, and the air temperature increased from −35.5 °C to −1.4 °C in the early phase of the storm but dropped quickly down to −30 °C (Fig. 2). Conditions led to ice break up and formation of multiple open water leads (Fig. 3A and B) with their subsequent freezing.

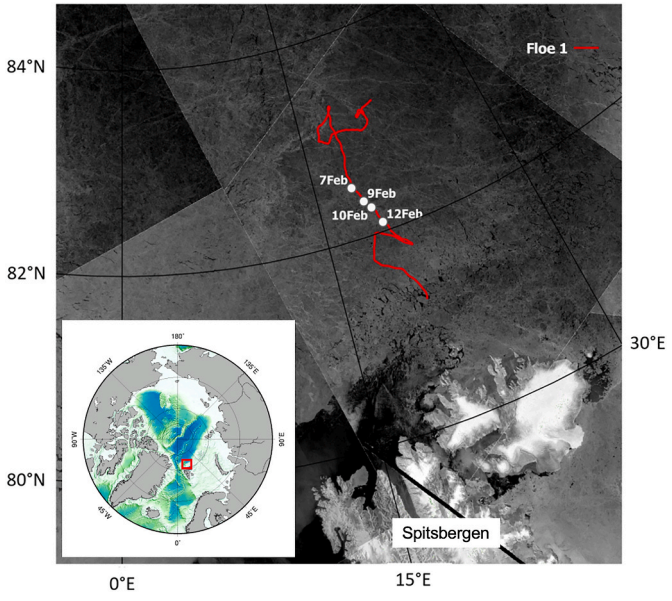

Fig. 1. (A) Drift track (red line) of R/V Lance during the N–ICE2015 campaign in January and February 2015, when it was anchored to Floe 1. White circles are positioned where ice coring in the lead took place. The background is from Copernicus Sentinel–1 satellite imagery (May 25, 2015; courtesy of European Space Agency) to indicate typical sea ice conditions in the study area. (For interpretation of the references to color in this figure legend, the reader is referred to the Web version of this article.)

Ice coring, seawater sampling, sea ice and snow observations (Rösel et al., 2018), and meteorological observations (Cohen et al., 2017) were accomplished from an ice camp situated on the ice floe 300–400 m away from the R/V Lance. Granskog et al. (2016, 2018) present a detailed description and motivation of the campaign.

2.2. Under–ice water sampling

Under–ice water was sampled using a Hydro–Bios SlimLine 6 CTD equipped with an integrated CT–set and six 3.5 L sample bottles before and after the storm on February 2, 3, 9, and 10. Sampling took place in a tent 400 m away from the ship. Seawater was collected from different depths from the surface down to 1000 m. Seawater for dissolved CH_4 analysis was transferred from the sample bottle into a 160 mL serum bottle using silicon tubing. Before filling, the bottles were rinsed three times with sample water, avoiding air bubbles. The sample was then poisoned with 50 μL of saturated $HgCl_2$, closed with isobutyl septa, crimped, and stored at +4 °C and dark until analysis. Under–ice water CH_4 concentrations are only reported for the upper 70 m below the sea ice.

2.3. Ice coring and sampling

New ice was sampled in two refrozen leads, and both are representative of the early ice formation (see Fig. 3 for the location of the two leads). Lead sampled on February 7 was a few tens meters wide. This floe area experienced divergent motion between February 2 and 7, and multiple fractures opened, closed, compressed, and sheared. A larger lead was sampled between February 9 and 12 (Fig. 3B). Six ice cores were collected on February 7, 9, and 10, and three on 12 (Table 1), given the homogeneous characteristics if this new ice, we believe this sampling provides appropriate representation of the ice cover in the leads over time. Ice cores on a single day were sampled 10–20 m apart along the edge of the lead. When the ice was thinner than 20 cm on February 7 and 9, a saw was used to cut out large squares of thin ice, which were temporarily placed in a bucket with an air–tight lid on for transportation to the ship and further processing. Before sampling, the ice temperature (T) was measured at the ice surface and in the middle of the ice using an electric drill and a calibrated probe (Testo 110 NTC, Brandt Instruments, Inc., USA). There were no ice T measurements on February 7. Therefore, assuming linear T gradient across thin ice, we estimated the ice T on

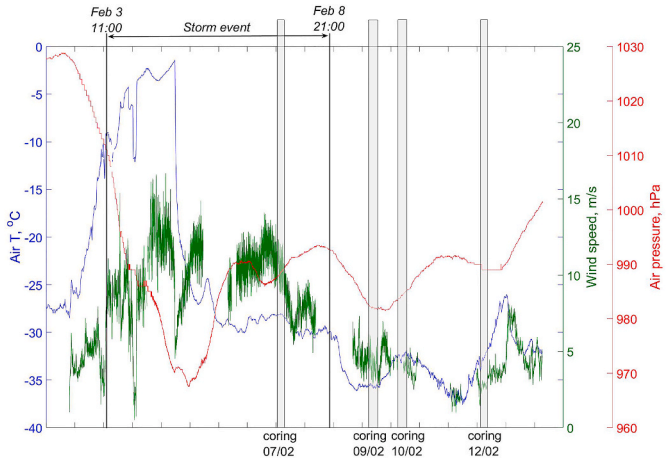

Fig. 2. Meteorological conditions (air temperature, air pressure, and wind speed) during the storm event and ice coring for this study. Periods of storm event and ice coring were also indicated.

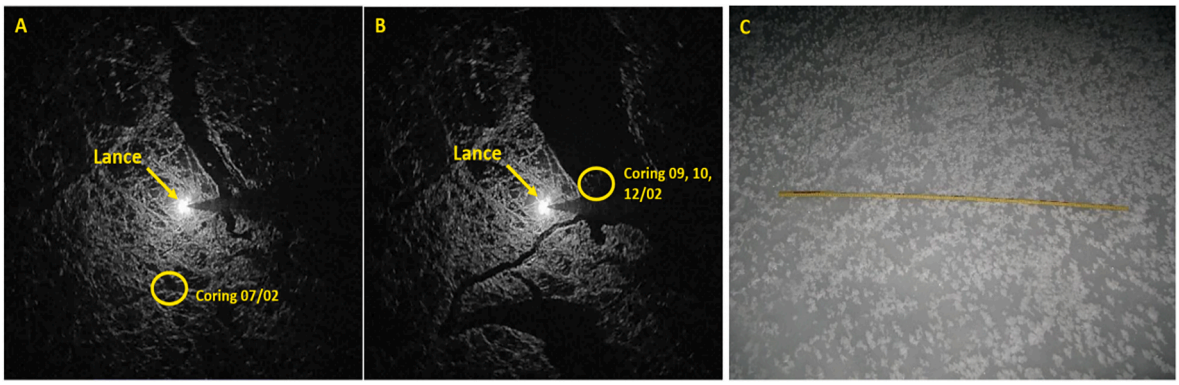

Fig. 3. Radar images of the sea ice surrounding R/V Lance, leads are areas with smooth black color while older sea ice with a rougher surface is shown by brighter shades taken from the ship–based radar (Haapala et al., 2017), on (A) February 7 and (B) February 9. The radar images are about 7 km across. (C) Photo of the frost flowers covered sea ice in the lead taken on February 9. A meter–stick in the photo is for scale. (For interpretation of the references to color in this figure legend, the reader is referred to the Web version of this article.)

Table 1
The list of sea ice cores collected in the leads, with dates, exact coordinates for each date, ice thickness (cm), average ice salinity, average ice temperature (°C), average CH_4 concentrations (nmol L^{-1}), air temperature (T, °C), wind speed (m s^{-1}), sea level pressure (hPa), number of section.

Date	Core ID	Time (UTC)	Ice thickness (cm)	Average salinity	Average ice T (°C)	Average CH_4 (nmol L^{-1})	Air T (°C)	Wind speed (m s^{-1})	Sea Level Pressure (hPa)	Number of sections
Feb. 7, 2015	C1	14:04	8	16.8	−4.6	6.2	−28.1	10.9	988	1
82.50 N	C2	14:14	8	15.3	−4.6	6.1	−28.2	10.7	988	1
17.81 E	C3	14:28	8	17.9	−4.6	6.7	−28.2	11.1	988	1
	C4	14:38	8	18.0	−4.6	7.1	−28.2	12.2	988	1
	C5	14:48	8	14.7	−4.6	7.2	−28.2	11.3	988	1
	C6	14:56	8	15.7	−4.6	5.4	−28.1	12.0	988	1
Feb. 9, 2015	C7	19:48	18	14.6	−14.1	7.6	−35.6	4.0	982	1
82.34 N	C8	19:56	17.5	15.4	−14.1	5.6	−35.4	5.3	982	1
18.39 E	C9	19:57	18	15.6	−14.1	4.0	−35.4	5.1	982	1
	C10	20:10	17.5	16.0	−14.1	4.4	−35.5	5.2	983	1
	C11	20:19	16.5	14.9	−14.1	4.8	−35.6	4.7	982	1
	C12	20:34	17.5	15.4	−14.1	5.6	−35.6	5.1	982	1
Feb. 10, 2015	C13	14:24	20.8	15.8	−11.8	4.5	−35.8	3.7	985	2
82.26 N	C14	14:31	21.4	16.2	−11.8	5.3	−35.7	5.2	985	2
18.79 E	C15	14:32	20	14.0	−14.15	5.4	−35.7	4.7	985	2
	C16	14:39	21.2	15.4	−11.8	3.8	−35.7	4.1	984	2
	C17	14:49	21	15.367	−11.8	3.8	−35.7	5.2	984	2
	C18	15:09	21.3	15.549	−11.8	7.5	−35.7	4.2	984	2
Feb. 12, 2015	C19	14:46	28	13.144	−11.1	5.2	−35.7	3.2	985	3
82.09 N	C20	15:20	27	11.803	−11.1	4.9	−36.0	4.5	984	3
19.25 E	C21	15:35	27	12.162	−11.1	4.1	−35.5	5.2	984	3

February 7 based on the T gradient measured on February 9 with bottom ice T of −1.9 °C, a freezing point at a salinity of 34.3 in under–ice surface waters on February 9.

For ice thicker than 20 cm (February 10 and 12), ice cores were collected using Kovacs ice corer with an internal diameter of either 9 or 14 cm (Mark II or Mark V, Kovacs Ent., Rosenburg, USA). Ice T was measured at every 10 cm of the core immediately after recovery. Each core for CH_4 measurements was cut into 10 cm sections and temporarily packed into Ziplock® bags for immediate transfer to R/V Lance. Onboard, all ice sections and pieces were immediately transferred into gas-tight Tedlar® plastic bags (5L Smart bag, GL Science, Japan), vacuumed by using a syringe, and left to melt at +4 °C in the dark. For CH_4 measurements, melted water from a gas–tight bag was transferred into a 60 ml serum bottle, using a silicon tube, poisoned with 50 μL of saturated $HgCl_2$, closed with isobutyl septa, crimped, and stored at +4 °C until analysis. For salinity measurements, melted water was put into glass bottles and measured onboard using a salinometer (Guildline 8410A, Canada) with an accuracy of ca. ±0.003.

2.4. Methane analysis

CH_4 concentrations in melted sea ice section (bulk ice CH_4 concentrations) and seawater samples were determined using the headspace technique within a few months after sampling (Upstill–Goddard et al., 1996). Headspace in melted sea ice samples, was analysed by a gas chromatograph (GC, SRI® 8610) equipped with a Flame Ionization Detector (FID). For gas chromatographic separation, we used a packed column (Hayesep D). The GC oven was operated isothermally (+50 °C), and the FID was held at +340 °C. After creating a 25 mL N_2 headspace in 60 mL glass serum bottles and 30 mL in 160 mL bottles, samples were vigorously shaken for 20 min and placed in a thermostatic bath overnight at −1.6 °C. The following day, the samples were shaken again for 20 min before the GC analysis. CH_4:CO_2:N_2O mixtures in the N_2 balance gas (Air Liquide, Belgium) of 1, 10, and 30 ppm of CH_4 were used to

create a three–point calibration curve for a standard. For under–ice seawater samples from February 2, 3, 9, and 10, we used gas chromatograph Agilent GC7890A with a FID. After creating 5 mL N_2 headspace in 160 mL serum bottles, samples were vigorously shaken on a shaker while brought to lab temperature (+20 °C). For gas chromatographic separation, we used a packed column (Porapac Q 80/100 mesh). The GC oven was operated isothermally (+60 °C), and the FID was held at +200 °C. Two sets of standard gas mixtures were used for calibration. The standard deviation of duplicate analyses was 5%. This overall error is almost exclusively due to the gas extraction procedure. The accuracy of the measurements by both instruments was within 3%. Final concentrations were computed using the CH_4 solubility coefficients given by Wiesenburg and Guinasso (1979).

2.5. CH_4 saturation and brine volume

CH_4 saturation in seawater, $CH_{4\ sat}$ (%) was computed following equation (1):

$$CH_{4\ sat} = (C_m/C^*) \cdot 100 \quad \text{(Eq. 1)}$$

where C_m is measured CH_4 concentration in seawater or sea ice, and C* is calculated CH_4 concentration at equilibrium with the atmosphere (4 nmol L^{-1}, with salinity, S = 34.3 and seawater temperature Tsw = −1.88 °C and atmospheric CH_4 mole fraction of 1900 ppb, Zeppelin Observatory, Svalbard on February 3, 2015) following Wiesenburg and Guinasso (1979). If $CH_{4\ sat}$ is higher than 100%, seawater or sea ice are CH_4 super–saturation and above equilibrium concentration with the atmosphere.

Brine volume fraction, as function of salinity and temperature, was calculated using in situ temperature and bulk salinity following Cox and Weeks (1983). Sea ice permeability is defined by a brine volume threshold of 5% (Golden et al., 1998). If brine volume is less than 5%, sea ice is impermeable.

2.6. Sea–to–air CH_4 flux calculations

The sea–to–air CH_4 flux F was calculated according to Wanninkhof et al. (2009):

$$F = k_{660} \cdot (C_m – C^*) \quad \text{(Eq. 2)}$$

where k_{660} is the calculated gas transfer velocity (cm hr^{-1} Table 2, Fig. 4; or m d^{-1} used in Eq. (2)), C*, and C_m are in nmol m^{-3}. k_{660} is normalized to a Schmidt number of 660, which is the ratio of water viscosity to molecular diffusivity.

For flux calculations in this study, we compare different parametrizations of gas transfer velocity k_{660} (Table 2 and Fig. 4), including scaling of k_{660} from Wanninkhof (2014) and Butterworth and Miller (2016) to the fraction of open water (f), which resulted in $k_{eff} = k_{660} \cdot f$ as suggested by Loose et al. (2014, 2016) and as in Butterworth and Miller (2016) for sea–ice zones. In Fig. 4, u indicated the measured wind speed at the meteorological mast at 10 m above the sea ice surface, which ranged between 0 and 25 m s^{-1}. Component f was calculated as the sea–ice fraction area subtracted from one. The sea–ice fraction was obtained from the AMSR2 microwave radiometer on the JAXA GCOM–W satellite. Sea–ice concentrations were derived from the 89 GHz channels, which allow a daily full global coverage of all sea–ice areas on a 6.25 × 6.25 km^2 grid (Spreen et al., 2008). The mean sea–ice concentration for a square of 43.75 × 43.75 km^2 (7 x 7 grid cells) with R/V Lance in the center pixel was calculated on an hourly basis. The GPS position of R/V Lance was used to identify the center grid cell in the ice concentration data set.

Table 2
Different k660 parameterizations.

Parameterization k_{660} (cm hr^{-1}); u (m s^{-1})	Source
$0.251 \cdot u^2$	Wanninkhof (2014)
$0.245 \cdot u^2 + 1.3$	Butterworth and Miller (2016)
$0.189 \cdot u^2$	Prytherch and Yelland (2021)
$0.251 \cdot u^2 \cdot f$	Wanninkhof (2014) scaled to f – open water fraction

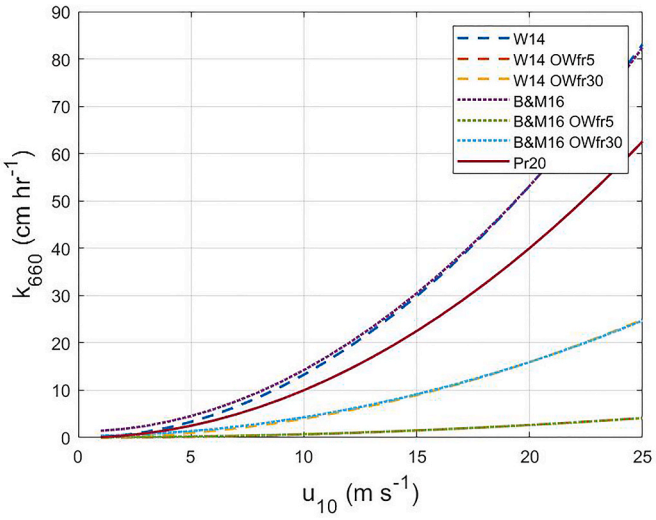

Fig. 4. Relationship of k660 to u10 based on parametrizations from Wanninkhof (2014) (W14), Butterworth and Miller (2016) (B&M 16), and Prytherch (2020) (Pr20). Owfr5 and Owfr30 are for open water fractions of 5 and 30% respectively, representing minimum and maximum open water fraction during 12 days of this study. u is the measured wind speed at the meteorological mast at 10 m above the sea ice surface, which ranged between 0 and 25 m s^{-1}.

Since there was no significant difference between W14 and B&M16 (Fig. 4), we present fluxes calculated with k_{660} parametrization for open water based on (1) Wanninkhof (2014), (W14), (2) k_{660} parametrization for mixed sea ice/open water (lead site) from Prytherch (2020), (Pr20), and (3) Wanninkhof (2014) taking into account open water fraction according to $k_{eff} = k_{660} \cdot f$ (W14 Owfr).

3. Results and discussion

3.1. CH_4 super–saturation in under–ice water

Observed under–ice water CH_4 concentration of 8–12 nmol L^{-1} equals $CH_{4\ sat}$ of 200–300%, which is super–saturation and above equilibrium concentration with the atmosphere (4 nmol L^{-1}, see Methods 2.5) (Fig. 5). This super–saturation is in agreement with observations of under–ice water below drifting sea ice from other AO regions (e.g., Kitidis et al., 2010; Damm et al., 2015a; Fenwick et al., 2017; Verdugo et al., 2021) and can potentially drive significant sea–to–air fluxes of CH_4.

3.2. Physico–chemical characteristics and methane evolution in newly formed sea ice

Newly formed sea ice rapidly covered open water leads following air temperature drop from −2 °C to −33 °C (Fig. 2). Once formed, this ice did not break as the meteorological conditions were stable (Fig. 2). The thickness of newly formed sea ice in the lead on February 7 was 8 cm, and in another lead increased from 18 to 27 cm in 4 days from February 9 to 12 (Figs. 6 and 7).

On the first day of observation (February 2), newly formed sea ice had high salinity (15–18, Fig. 6A), high temperature for the top (−7.2 °C, Fig. 6B), and high brine volume for top (10–13%, Fig. 6C) with respect to those on the subsequent days. This is typical for young ice forming over open leads in winter (Perovich and Gow, 1996). This ice

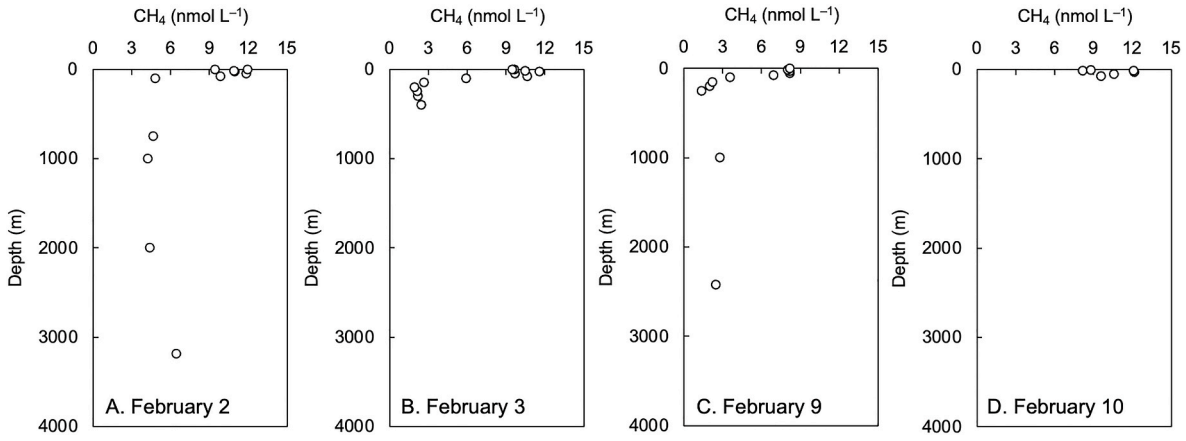

Fig. 5. Methane concentrations in under–ice water sampled on (A) February 2, (B) February 3, (C) February 9, and (D) February 10. Water on all these days was sampled from under sea ice and not from the ice edge.

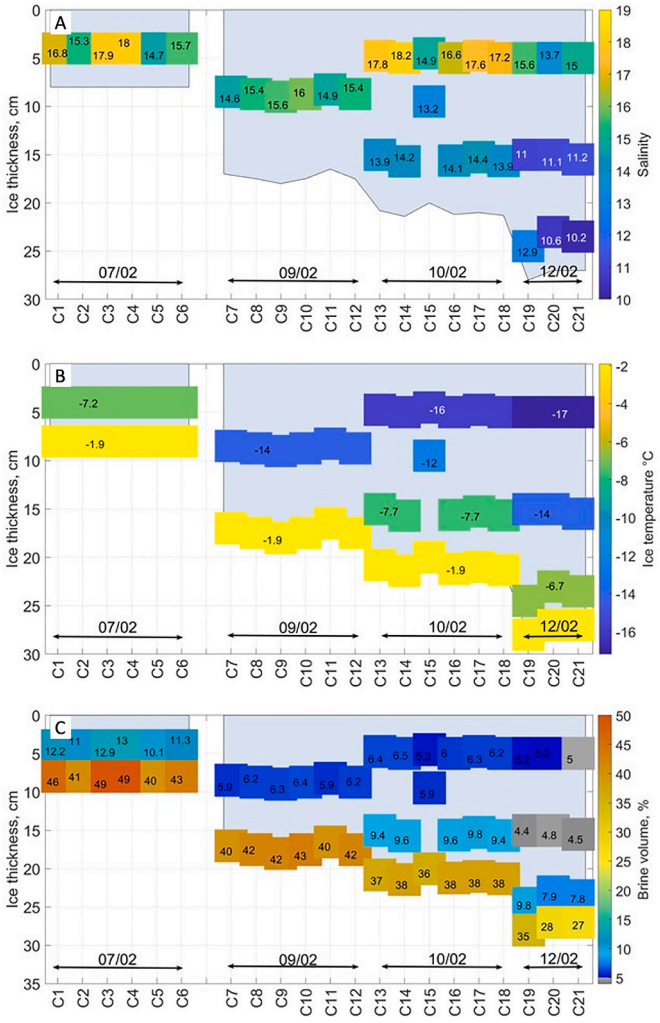

Fig. 6. (A) Sea ice salinity, (B) ice temperature, and (C) and brine volume fraction for ice core of C1–C21 (Table 1 for reference). The light blue background shows the sea ice thickness. Grey in (C) indicates values equal or below 5%, which is a threshold for sea ice permeability. (For interpretation of the references to color in this figure legend, the reader is referred to the Web version of this article.)

was very porous, which allows gas exchange through the growing ice since it highly permeable. Gases dissolved in brine are rejected downward to under–ice water together with brine during ice formation (e.g., Weeks and Ackley, 1986; Vancoppenolle et al., 2013) but at same rate as salts. This is implied by the lower sea ice salinity at the bottom ice section on February 12 (salinity 10–12), which grew later when compared to top horizons (salinity 13–17) (Fig. 6A). Higher CH_4 concentrations in bottom ice sections compared to top horizons (Fig. 7A) suggest the downward movement of CH_4 containing brine (Damm et al., 2015b). On the other hand, higher CH_4 concentrations in the bottom ice sections could also be explained by the fact that new ice grown underneath contains a high amount of CH_4 from supersaturated under–ice seawater. However, diffusive gas flux from under–ice water into the sea ice (across the concentration gradient between "brine" in bottom of sea ice and under-ice water) was shown to be negligible (2%, Lovely et al., 2015) and hence is unlikely to contribute to higher CH_4 concentrations in bottom sections of growing sea ice.

The top of the ice was covered with frost flowers (Fig. 3C), which is a sign of brine being expelled upwards to the ice surface (e.g., Perovich and Richter-Menge, 1994; Barber et al., 2014) and gases leaving sea ice into the atmosphere (Fransson et al., 2015; Granfors et al., 2013; Nomura et al., 2018). Higher salinity in the top of the ice compared to bottom horizons was observed in this study (Fig. 6A), even in later days of observations, could indicate upward ejection of brine (Kaleschke et al., 2004). At the same time, the CH_4 concentration decreases (from 5 to 7 nmol L^{-1} to 4 nmol L^{-1} over five days (Fig. 7A) and CH_4 to salinity ratio decrease in top horizons of newly formed sea ice (Fig. 7B) suggests that upper layers lost CH_4 into the atmosphere relative to salts. CH_4 release to the atmosphere occurs due to the diffusion of dissolved gas through the equilibration between the brine in the top of the ice and the atmosphere without exchange of salt. Also, CH_4 containing buoyant bubbles that are trapped in seawater during sea–ice formation travel upward in the ice through brine channels and release to the atmosphere (e.g., Loose et al., 2009, 2011; Crabeck et al., 2014). Moreover, bubbles are formed within sea ice structure when CH_4 solubility lowers due to the increase of salinity in brines (Zhou et al., 2013, 2014). Bubble formation is likely to be enhanced in young ice as there is still a large volume of concentrated salty brine that lowers solubility (Zhou et al., 2013), and the ice is permeable. As brine volumes stayed significantly higher than the 5% permeability threshold in the upper layer of the ice for all sampling days (Fig. 6C), there was a potential for continuous CH_4 evasion from the brine in the upper ice horizons. Based on our observations, we surmise that the thin ice formed after the winter storm was porous and an active source of CH_4 into the atmosphere. This finding agrees with elevated CO_2 fluxes from thin ice observed by Nomura et al. (2018).

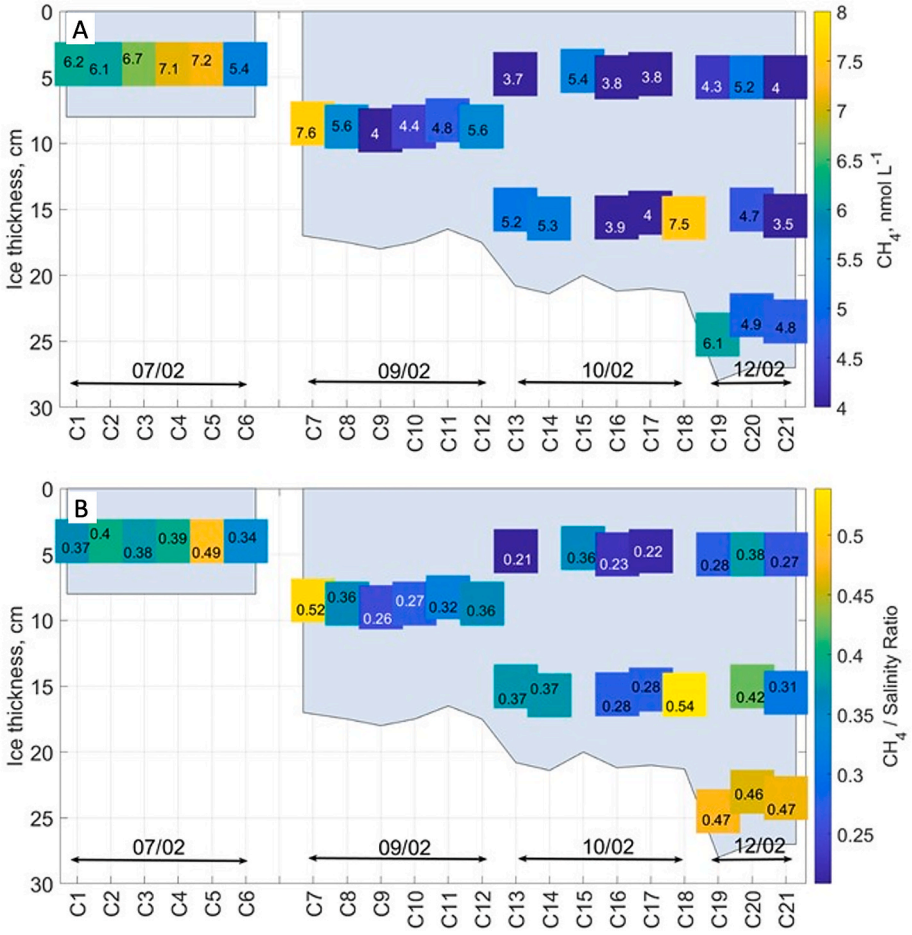

Fig. 7. (A) Sea ice CH_4 concentration and (B) CH_4 concentration to salinity ratio for ice core of C1–C21 (Table 1 for reference). The light blue background shows the sea ice thickness. (For interpretation of the references to color in this figure legend, the reader is referred to the Web version of this article.)

3.3. Sea–to–air CH_4 flux in open leads

Open water leads frequently appeared between the beginning of the storm on February 3 and the last day of ice coring in this study on February 12, as indicated from radar images (Haapala et al., 2017). During the storm, calculated mean sea–to–air CH_4 flux from these open water leads was +0.31 mg CH_4 m^{-2} d^{-1} with a maximum flux of +1.59 mg CH_4 m^{-2} d^{-1} with a surface water CH_4 concentration of 10 nmol L^{-1} (based on open water parametrization of k_{660} W14, Fig. 5 top, Table 3) (Fig. 8). For the calmer post–storm conditions, the mean CH_4 flux was +0.08 mg CH_4 m^{-2} d^{-1}, and the maximum flux was +0.13 mg CH_4 m^{-2} d^{-1}. Thus, the highest flux was estimated during the storm at high wind speeds. After the storm, in calmer weather, the flux from open leads decreased as wind speeds decreased, and the leads froze over (Fig. 8).

In the open ocean, where the difference between surface water and atmospheric CH_4 concentrations is not very large, the flux depends mainly on wind speed, since the deciding part of the equation, the gas transfer velocity k_{660}, depends on wind speed. Comparing five different k_{660} parametrizations for the open ocean, Graves et al. (2015) concluded that different k_{660} parametrizations yield overall sea–to–air CH_4 fluxes ranging from 20 to 35% lower and 30–75% higher than mean flux, depending on the wind speed.

Flux calculations in the open leads show the same as in the open ocean dependency on wind speed. Prytherch and Yelland (2021) proposed that gas transfer in sea ice–covered areas mixed with open water leads is decreased by 25% relative to the open ocean (based on eddy

Table 3
CH_4 fluxes calculated with different k660 parametrizations. Fluxes are calculated as maximum, minimum, and mean values for the storm event (3–8 February) and post–storm low winds.

		Storm event (winds >7 m s^{-1})			Still, no storm (winds <7 m s^{-1})		
		8 nmol L^{-1}	10 nmol L^{-1}	12 nmol L^{-1}	8 nmol L^{-1}	10 nmol L^{-1}	12 nmol L^{-1}
k_{660} W14	Max	1.04	1.59	2.13	0.09	0.13	0.18
	Min	0.01	0.02	0.02	0.02	0.03	0.03
	Mean	0.20	0.31	0.41	0.05	0.08	0.10
k_{660} Pr20	Max	0.79	1.20	1.60	0.07	0.10	0.14
	Min	0.01	0.01	0.02	0.01	0.02	0.03
	Mean	0.15	0.23	0.31	0.04	0.06	0.08
k_{660} W14OW fr	Max	0.10	0.15	0.20	0.02	0.03	0.05
	Min	0	0	0.01	0	0	0
	Mean	0.03	0.04	0.06	0	0.01	0.02

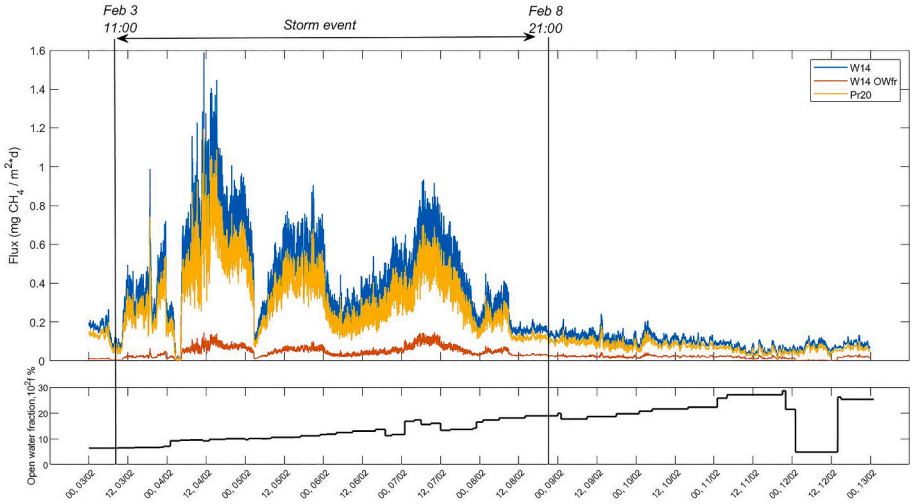

Fig. 8. Calculated sea–to–air fluxes of CH_4 (top panel) using a surface CH_4 concentration of 10 nmol L^{-1}, with three different k660 parametrizations as in Table 2, bold font. Open water fractions in percent (bottom panel).

covariance measurements of CO_2 fluxes in the central AO). Using Pr20, we calculated mean and maximum CH_4 fluxes during the storm as 0.23 and 1.20 mg CH_4 m^{-2} d^{-1}, respectively, while in calm weather as 0.06 and 0.1 mg CH_4 m^{-2} d^{-1} respectively (Fig. 8).

In the presence of sea ice, Loose et al. (2014, 2016) suggested that air–sea gas exchange not only depends on wind speed but on sea–ice fraction itself, surface water currents, and convection–driven turbulent mixing. The latter two are suggested to drive the air–sea gas exchange in the way of replenishing surface waters supplying excess gas to surface water open to the air, thus more gas to be released into the atmosphere (Damm et al., 2007, 2015a; Lovely et al., 2015; Loose et al., 2016). Prytherch and Yelland (2021) observed, however, that this convection–driven turbulent mixing is less likely to influence gas exchange in the sea ice–covered areas with open leads in the central AO in late summer.

Following the approach of scaling CH_4 flux to the open water fraction (Loose et al., 2014) implies that CH_4 transfer only occurs in the open water leads. During the storm event in this study, the open water fraction around R/V Lance in an area of 43.75 km^2 increased from 5 to 30% (Fig. 4). Fluxes scaled to the open water fraction (W14 OWfr) were 91 and 87% lower than fluxes based on open water parametrization W14 and sea ice/open leads parametrization Pr20, respectively (Table 3) because scaling CH_4 flux to the open water fraction (W14 OWfr) does not take into account the CH_4 exchange for the sea ice area, and the presence of sea ice reduces the gas exchange process. Therefore, Pr20 parametrization is valid for our study area, which also had a sea ice cover with open water leads.

Scaling CH_4 flux to the open water fraction implies that no CH_4 exchange occurs through sea ice (Kitidis et al., 2010). Despite the upward diffusion of gas from under–ice water to sea ice might be negligible (Lovely et al., 2015), direct measurements of CO_2 fluxes on sea ice suggested that gas exchange through the brine channels within sea ice is significant (e.g., Delille et al., 2014; Nomura et al., 2018). However, similar direct measurements for CH_4 fluxes are few. He et al. (2013) (summer in central AO, −0.94 to +0.77 mg CH_4 m^{-2} d^{-1}) and Nomura et al. (2020, 2022) (Lake Saroma, +0.01 mg CH_4 m^{-2} d^{-1}) measured CH_4 fluxes from sea ice to the atmosphere with the chamber technique. Remarkably, measurements in the central AO indicate not only positive but also negative CH_4 flux, implying that sea ice is not always a source but can also be a sink for atmospheric CH_4 since sea ice has lost CH_4 to the atmosphere (and partly ocean below), it can become a potential sink. In addition, especially summer-time, snow/sea ice meltwater dilute the CH_4 at the surface of sea ice and decreases CH_4 concentration with respect to the atmosphere. Therefore, sea ice could act as a potential sink for atmospheric CH_4. This CH_4 seasonal variation agrees with that of CO_2 concentration within the sea ice and flux between sea ice and atmosphere (e.g., Delille et al., 2014).

Despite the evidence of CH_4 exchange across the surface of sea ice, most studies reporting marine CH_4 fluxes in the AO are based on k_{660} parametrizations for the open ocean in the ice–free zones and assume no CH_4 flux through the sea ice cover (Table 4). Moreover, it appears that the CH_4 flux is higher in AO regions with CH_4 supersaturated surface waters (Thornton et al., 2016) connected to a geological sources. Areas with degrading subsea permafrost as the Laptev, East Siberian, and Chukchi Seas emit the most CH_4 to the atmosphere in ice–free conditions (on average 1.5–3.8 mg CH_4 m^{-2} d^{-1}, Thornton et al., 2016, 2020) as they have the greatest yet reported CH_4 concentrations in surface waters (e.g., 100 times above equilibrium, Shakhova et al., 2010). In the wintertime, there are also large gas bubbles trapped within the sea ice, and bubbles presumably consist of CH_4, but ice–air fluxes have not been measured. Several observations of under–ice CH_4 concentrations in different parts of the AO (Kvenvolden et al., 1993; Thornton et al., 2016) speculate that the CH_4 flux into the atmosphere is a seasonal feature occurring as a one–time event when the ice melts or breaks as in the case of smaller shallower northern lakes (e.g., Engram et al., 2020). However, this is obviously not the case for the dynamic and mobile pack ice. Flux from ice–covered but fractured AO areas in the Chukchi and East Siberian seas, the areas, which are close to geological CH_4 sources, has been reported to be relatively high in summer when ice concentrations decrease due to ice melt (2 mg CH_4 m^{-2} d^{-1}, Kort et al., 2012), implying that sea ice dynamics and fracturing could play a significant role in the AO becoming a larger marine source of CH_4 into the atmosphere than previously estimated (e.g., Parmentier et al., 2015). Moreover, as shown in this study, newly formed sea ice in winter also emits CH_4 into the lower atmosphere. This puts emphasis on the importance of studies of CH_4 dynamics in sea ice, also in winter when the ice concentration is high and fracturing of the ice pack and subsequent new ice formation can result in increased potential for CH_4 evasion to the atmosphere.

4. Conclusions

We observed methane (CH_4) dynamics in under–ice water and new thin sea ice in the Nansen Basin of the Arctic Ocean (AO) following a winter storm. The many new fractures in the ice pack, initially areas of open water leads became consequently large areas of new thin and permeable sea ice, formed as a result of this storm (similar to that observed for a later storm the same winter (Itkin et al., 2018). During storm–induced ice break up, CH_4 vented into the air from supersaturated

Table 4
Sea–to–air fluxes (mg CH_4 m^{-2} d^{-1}) in different areas of the AO. All values are positive (flux from the ocean to atmosphere).

Source	Flux	Latitude	Longitude	Season or month	Sea ice conditions	Location/region	Method used
This study	0.23	82.08	19.25	winter (Feb.)	ice covered with leads open	Nansen basin	Calculated based on Wanninkhof (2014)
Shakhova et al. (2010)	3.67	75.04	128.74	summer	ice–free	Laptev Sea (mean)	Calculated based on Wanninkhof (1992)
Thornton et al. (2016)	3.80	73.16	166.10	summer	ice–free	Western East Siberian Sea	Calculated based on Wanninkhof, 2014
Thornton et al. (2020)	1.50	–	–	summer	Mixed ice covered/ ice free	Laptev + East Siberian + Chukchi seas	Eddy covariance measurements
Kort et al. (2012)	2.00	82.53	145.00	Nov., Apr.	ice covered with leads open	North of Alaska	Estimations based on air mole fraction ppm and eddy diffusivity 0.3 m^{-2} s^{-1}
He et al. (2013)	0.56	86.81	173.24	summer	ice–covered	Central Arctic Ocean	Chamber technique measurements
Damm et al. (2007)	1.05	77.31	19.35	Mar.	polynya	Storfjorden Polynya	Calculated based on Wanninkhof (1992)
Silyakova et al. (2020)	0.24	78.38	10.48	summer	ice–free	West Spitsbergen	Calculated based on Wanninkhof et al., 2009
Graves et al. (2015)	0.32	78.55	9.42	summer	ice–free	West Spitsbergen	Calculated based on Wanninkhof et al., 2009
Lammers et al. (1995)	0.08	74.90	27.56	Aug.	ice–free	Barents Sea	Calculated based on Wanninkhof (1992)

under–ice water (8–12 nmol L^{-1}) in open water leads (up to 30% of overall surface area) with a maximum flux of 1.04–2.13 mg CH_4 m^{-2} d^{-1}. Initially, newly formed sea ice in the leads was CH_4 supersaturated with respect to the atmosphere (5–7 nmol L^{-1}). During five days of observations, 2–3 nmol L^{-1} of this CH_4 escaped into the atmosphere until concentrations equilibrated with the atmosphere, and the ice became less permeable. This implies that the winter ice pack is not an impermeable barrier for CH_4 loss to the atmosphere, and not only the open water leads but also the sea ice itself plays an active role in this wintertime flux.

Understanding of CH_4 dynamics and associated processes in different sea ice conditions as well as under various meteorological events becomes an essential link for better estimates of CH_4 emissions from the CH_4 supersaturated AO surface waters and sea ice into the atmosphere. Sea ice is entering a new state from being largely thicker multi–year sea ice to predominantly thinner first–year thinner sea ice (Maslanik et al., 2011; Stroeve et al., 2012; Meier et al., 2014). Moreover, increasing the mean speed and deformation rate of the Arctic sea ice (Spreen et al., 2011), and rising frequency of winter storms and warming events in the Arctic (Graham et al., 2017, 2019) lead to an increasing amount of occurring fractures and open water leads. All these factors in addition to decreasing sea ice concentration in the AO, may enhance gas transfer intensity similar to what has been shown for CO_2 (Prytherch et al., 2017). The release of CH_4 into the atmosphere could be substantial in the future AO and is opposed to the scenario when CH_4 is majorly consumed by microbes while residing beneath sea ice cover (Kitidis et al., 2010). It is said that the CH_4 release rate from the East Siberian Sea estimated from atmospheric observations indicates that the bottom-up estimates could be overestimated (Tohjima et al., 2021). In–depth multidisciplinary studies of changes in the coupled ocean–ice–atmosphere system with a focus on CH_4 dynamics and exchange will shed light on whether the AO itself is a more significant source of atmospheric CH_4 than previously thought (Myhre et al., 2016).

Declaration of competing interest

The authors declare that they have no known competing financial interests or personal relationships that could have appeared to influence the work reported in this paper.

Acknowledgments

We thank the captain, engineers, and crew of R/V Lance for technical and logistic support during the entire N–ICE2015 expedition. We thanks Paul Dodd for help with the sampling of thin ice and under–ice water; Jari Haapala for providing a time–lapse of radar images from the dataset; Ellen Damm for measurements of dissolved CH_4 concentrations in under–ice water samples, and insightful discussions at early stage of this manuscript preparation; and Gunnar Spreen for providing sea–ice fraction area data. The N–ICE2015 expedition was supported by the N–ICE project at the former Centre for Ice, Climate and Ecosystems at the Norwegian Polar Institute. This study is a part of the CAGE (Centre for Arctic Gas Hydrate, Environment, and Climate), Norwegian Research Council grant no. 223259. Part of the field work and sampling was funded by the Flagship research program “Ocean Acidification and effects in northern waters” within the FRAM– High North Research Centre for Climate and the Environment (AF). This work was supported by the Japan Society for the Promotion of Science (15K16135,17H04715, 18H03745, 20H04345). MK and BD are PhD students and research associate, respectively, of the F.R.S.–FNRS. The N–ICE2015 expedition was supported by the N–ICE project at the former Centre for Ice, Climate and Ecosystems at the Norwegian Polar Institute. This study is a part of the CAGE (Centre for Arctic Gas Hydrate, Environment, and Climate), Norwegian Research Council grant no. 223259. Part of the field work and sampling was funded by the Flagship research program “Ocean Acidification and effects in northern waters” within the FRAM–High North Research Centre for Climate and the Environment (AF). MK and BD are PhD students and research associate, respectively, of the F.R.S.–FNRS. The data supporting the conclusions of this study are freely available at the Norwegian Polar Data Centre (data.npolar.no) and should be cited as Silyakova, A., Kotovich, M., Fransson, A., Nomura, D., Delille, B., Damm, E., Chierici, M., and Granskog, M. A. (2022). N–ICE2015 methane concentrations in new sea ice and under–ice water [Data set]. Norwegian Polar Institute. https://doi.org/10.21334/npolar.2022.9ef02026.

References

Asplin, M.G., Scharien, R., Else, B., Howell, S., Barber, D.G., Papakyriakou, T., Prinsenberg, S., 2014. Implications of fractured Arctic perennial ice cover on thermodynamic and dynamic sea ice processes. J. Geophys. Res.: Oceans 119 (4), 2327–2343.

Barber, D.G., Ehn, J.K., Pućko, M., Rysgaard, S., Deming, J.W., Bowman, J.S., Søgaard, D. H., 2014. Frost flowers on young Arctic sea ice: the climatic, chemical, and microbial significance of an emerging ice type. J. Geophys. Res. Atmos. 119 (20), 11–593.

Butterworth, B.J., Miller, S.D., 2016. Air–sea exchange of carbon dioxide in the Southern Ocean and Antarctic marginal ice zone. Geophys. Res. Lett. 43 (13), 7223–7230.

Cohen, L., Hudson, S.R., Walden, V.P., Graham, R.M., Granskog, M.A., 2017. Meteorological conditions in a thinner Arctic sea ice regime from winter to summer during the Norwegian Young Sea Ice expedition (N–ICE2015). J. Geophys. Res. Atmos. 122 (14), 7235–7259.

Cox, G.F., Weeks, W.F., 1983. Equations for determining the gas and brine volumes in sea–ice samples. J. Glaciol. 29 (102), 306–316.

Crabeck, O., Delille, B., Rysgaard, S., Thomas, D.N., Geilfus, N.X., Else, B., Tison, J.L., 2014. First ''in situ'' determination of gas transport coefficients (D_{O2}, D_{Ar}, and D_{N2}) from bulk gas concentration measurements (O_2, N_2, Ar) in natural sea ice. J. Geophys. Res.: Oceans 119 (10), 6655–6668.

Damm, E., Bauch, D., Krumpen, T., Rabe, B., Korhonen, M., Vinogradova, E., Uhlig, C., 2018. The transpolar drift conveys methane from the siberian shelf to the central Arctic Ocean. Sci. Rep. 8 (1), 1–10.

Damm, E., Helmke, E., Thoms, S., Schauer, U., Nöthig, E., Bakker, K., Kiene, R.P., 2010. Methane production in aerobic oligotrophic surface water in the central Arctic Ocean. Biogeosciences 7 (3), 1099–1108.

Damm, E., Rudels, B., Schauer, U., Mau, S., Dieckmann, G., 2015b. Methane excess in Arctic surface water–triggered by sea ice formation and melting. Sci. Rep. 5, 16179.

Damm, E., Schauer, U., Rudels, B., Haas, C., 2007. Excess of bottom–released methane in an Arctic shelf sea polynya in winter. Continent. Shelf Res. 27 (12), 1692–1701.

Damm, E., Thoms, S., Beszczynska–Möller, A., Nöthig, E.M., Kattner, G., 2015a. Methane excess production in oxygen–rich polar water and a model of cellular conditions for this paradox. Polar Sci. 9 (3), 327–334.

Delille, B., Vancoppenolle, M., Geilfus, N.X., Tilbrook, B., Lannuzel, D., Schoemann, V., Chou, L., 2014. Southern Ocean CO_2 sink: the contribution of the sea ice. J. Geophys. Res.: Oceans 119 (9), 6340–6355.

Engram, M., Anthony, K.W., Sachs, T., Kohnert, K., Serafimovich, A., Grosse, G., Meyer, F.J., 2020. Remote sensing northern lake methane ebullition. Nat. Clim. Change 10 (6), 511–517.

Fenwick, L., Capelle, D., Damm, E., Zimmermann, S., Williams, W.J., Vagle, S., Tortell, P. D., 2017. Methane and nitrous oxide distributions across the North American Arctic Ocean during summer, 2015. J. Geophys. Res.: Oceans 122 (1), 390–412.

Fransson, A., Chierici, M., Abrahamsson, K., Andersson, M., Granfors, A., Gårdfeldt, K., Torstensson, A., Wulff, A., 2015. Development of the CO_2 system in young and new sea ice and CO_2–gas exchange at the ice–air interface through brine transport and frost flowers in Kongsfjorden, Svalbard. Ann. Glaciol. 56 (69), 245–257. https://doi.org/10.3189/2015AoG69A563.

Fransson, A., Chierici, M., Skjelvan, I., Olsen, A., Assmy, P., Peterson, A.K., Ward, B., 2017. Effects of sea–ice and biogeochemical processes and storms on under–ice water fCO_2 during the winter–spring transition in the high Arctic Ocean: implications for sea–air CO_2 fluxes. J. Geophys. Res.: Oceans 122 (7), 5566–5587.

Golden, K.M., Ackley, S.F., Lytle, V.I., 1998. The percolation phase transition in sea ice. Science 282 (5397), 2238–2241.

Graham, R.M., Cohen, L., Petty, A.A., Boisvert, L.N., Rinke, A., Hudson, S.R., Granskog, M.A., 2017. Increasing frequency and duration of Arctic winter warming events. Geophys. Res. Lett. 44 (13), 6974–6983.

Graham, R.M., Itkin, P., Meyer, A., Sundfjord, A., Spreen, G., Smedsrud, L.H., Fer, I., 2019. Winter storms accelerate the demise of sea ice in the Atlantic sector of the Arctic Ocean. Sci. Rep. 9 (1), 1–16.

Granfors, A., Andersson, M., Chierici, M., Fransson, A., Gårdfeldt, K., Torstensson, A., Wulff, A., Abrahamsson, K., 2013. Biogenic halocarbons in young Arctic sea ice and frost flowers – sources of atmospheric halogens. Mar. Chem. 155, 124–134. https://doi.org/10.1016/j.marchem.2013.06.002.

Granskog, M.A., Assmy, P., Gerland, S., Spreen, G., Steen, H., Smedsrud, L.H., 2016. Arctic research on thin ice: consequences of Arctic sea ice loss. Eos Trans. AGU 97 (5), 22–26.

Granskog, M.A., Fer, I., Rinke, A., Steen, H., 2018. Atmosphere–ice–ocean–ecosystem processes in a thinner Arctic Sea ice regime: the Norwegian Young Sea ICE (N–ICE2015) Expedition. J. Geophys. Res.: Oceans 123 (3), 1586–1594.

Graves, C.A., Steinle, L., Rehder, G., Niemann, H., Connelly, D.P., Lowry, D., James, R.H., 2015. Fluxes and fate of dissolved methane released at the seafloor at the landward limit of the gas hydrate stability zone offshore western Svalbard. J. Geophys. Res.: Oceans 120 (9), 6185–6201.

Haapala, J., Oikkonen, A., Gierisch, A., Itkin, P., Nicolaus, M., Spreen, G., Lensu, M., 2017. N–ICE2015 Ship Radar Images [Data Set]. Norwegian Polar Institute. https://doi.org/10.21334/npolar.2017.6441ca81.

He, X., Sun, L., Xie, Z., Huang, W., Long, N., Li, Z., Xing, G., 2013. Sea ice in the Arctic Ocean: role of shielding and consumption of methane. Atmos. Environ. 67, 8–13.

Itkin, P., Spreen, G., Cheng, B., Doble, M., Girard–Ardhuin, F., Haapala, J., Wilkinson, J., 2017. Thin ice and storms: sea ice deformation from buoy arrays deployed during N–ICE2015. J. Geophys. Res.: Oceans 122 (6), 4661–4674.

Itkin, P., Spreen, G., Hvidegaard, S.M., Skourup, H., Wilkinson, J., Gerland, S., Granskog, M.A., 2018. Contribution of deformation to sea ice mass balance: a case study from an N–ICE2015 storm. Geophys. Res. Lett. 45 (2), 789–796.

Kaleschke, L., Richter, A., Burrows, J., Afe, O., Heygster, G., Notholt, J., Jacobi, H.W., 2004. Frost flowers on sea ice as a source of sea salt and their influence on tropospheric halogen chemistry. Geophys. Res. Lett. 31 (16).

Kitidis, V., Upstill–Goddard, R.C., Anderson, L.G., 2010. Methane and nitrous oxide in surface water along the north–west passage, Arctic Ocean. Mar. Chem. 121 (1–4), 80–86.

Kort, E.A., Wofsy, S.C., Daube, B.C., Diao, M., Elkins, J.W., Gao, R.S., Spackman, J.R., 2012. Atmospheric observations of Arctic Ocean methane emissions up to 82 north. Nat. Geosci. 5 (5), 318–321.

Kvenvolden, K.A., Lilley, M.D., Lorenson, T.D., Barnes, P.W., McLaughlin, E., 1993. The Beaufort Sea continental shelf as a seasonal source of atmospheric methane. Geophys. Res. Lett. 20 (22), 2459–2462.

Lammers, S., Suess, E., Hovland, M., 1995. A large methane plume east of Bear Island (Barents Sea): implications for the marine methane cycle. Geol. Rundsch. 84 (1), 59–66.

Loose, B., McGillis, W.R., Schlosser, P., Perovich, D., Takahashi, T., 2009. Effects of freezing, growth, and ice cover on gas transport processes in laboratory seawater experiments. Geophys. Res. Lett. 36, L05603 https://doi.org/10.1029/2008GL036318.

Loose, B., Lovely, A., Schlosser, P., Zappa, C., McGillis, W., Perovich, D., 2016. Currents and convection cause enhanced gas exchange in the ice–water boundary layer. Tellus B 68 (1), 32803.

Loose, B., McGillis, W.R., Perovich, D., Zappa, C.J., Schlosser, P., 2014. A parameter model of gas exchange for the seasonal sea ice zone. Ocean Sci. 10 (1), 17–28.

Loose, B., Schlosser, P., Perovich, D., Ringelberg, D., Ho, D.T., Takahashi, T., Tison, J.L., 2011. Gas diffusion through columnar laboratory sea ice: implications for mixed–layer ventilation of CO_2 in the seasonal ice zone. Tellus B 63 (1), 23–39.

Lovely, A., Loose, B., Schlosser, P., McGillis, W., Zappa, C., Perovich, D., Friedrich, R., 2015. The gas transfer through Polar Sea ice experiment: insights into the rates and pathways that determine geochemical fluxes. J. Geophys. Res.: Oceans 120 (12), 8177–8194.

Maslanik, J., Stroeve, J., Fowler, C., Emery, W., 2011. Distribution and trends in Arctic sea ice age through spring 2011. Geophys. Res. Lett. 38 (13).

Meier, W.N., Hovelsrud, G.K., Van Oort, B.E., Key, J.R., Kovacs, K.M., Michel, C., Makshtas, A., 2014. Arctic sea ice in transformation: a review of recent observed changes and impacts on biology and human activity. Rev. Geophys. 52 (3), 185–217.

Myhre, C.L., Ferré, B., Platt, S.M., Silyakova, A., Hermansen, O., Allen, G., Mienert, J., 2016. Extensive release of methane from Arctic seabed west of Svalbard during summer 2014 does not influence the atmosphere. Geophys. Res. Lett. 43 (9), 4624–4631.

Nomura, D., Granskog, M.A., Fransson, A., Chierici, M., Silyakova, A., Ohshima, K.I., Dieckmann, G.S., 2018. CO_2 flux over young and snow–covered Arctic pack ice in winter and spring. Biogeosciences 15 (11), 3331–3343.

Nomura, D., Wongpan, P., Toyota, T., Tanikawa, T., Kawaguchi, Y., Ono, T., Son, E.Y., 2020. Saroma–ko lagoon observations for sea ice physico–chemistry and Ecosystems 2019 (SLOPE2019). Bull. Glaciol. Res. 38, 1–12. https://doi.org/10.5331/bgr.19R02.

Nomura, D., Ikawa, H., Kawaguchi, Y., Kanna, N., Kawakami, T., Nosaka, Y., Umezawa, S., Tozawa, M., Horikawa, T., Sahashi, R., Noshiro, T., Kaba, I., Ozaki, M., Kondo, F., Ono, K., Yabe, I.S., Son, E.Y., Toyoda, T., Kameyma, S., Wang, C., Obata, H., Ooki, A., Ueno, H., Kasai, A., 2022. Atmosphere–sea ice–ocean interaction study in Saroma-ko Lagoon, Hokkaido, Japan. Bull. Glaciol. Res. 40, 1–17. https://doi.org/10.5331/bgr.21R02.

Parmentier, F.J.W., Silyakova, A., Biastoch, A., Kretschmer, K., Panieri, G., 2015. Natural marine methane sources in the Arctic. Arctic Monit. Assess. Programme (AMAP) 27–38. ISBN 978-82-7971-091-2.

Paull, C.K., Ussler, W., Dallimore, S.R., Blasco, S.M., Lorenson, T.D., Melling, H., McLaughlin, F.A., 2007. Origin of pingo–like features on the Beaufort Sea shelf and their possible relationship to decomposing methane gas hydrates. Geophys. Res. Lett. 34 (1).

Perovich, D.K., Gow, A.J., 1996. A quantitative description of sea ice inclusions. J. Geophys. Res.: Oceans 101 (C8), 18327–18343.

Perovich, D.K., Richter–Menge, J.A., 1994. Surface characteristics of lead ice. J. Geophys. Res. 99 (C8), 16341–16350.

Platt, S.M., Eckhardt, S., Ferré, B., Fisher, R.E., Hermansen, O., Jansson, P., Silyakova, A., 2018. Methane at svalbard and over the European Arctic Ocean. Atmos. Chem. Phys. 18 (23), 17207–17224.

Portnov, A., Smith, A.J., Mienert, J., Cherkashov, G., Rekant, P., Semenov, P., Vanshtein, B., 2013. Offshore permafrost decay and massive seabed methane escape in water depths> 20 m at the South Kara Sea shelf. Geophys. Res. Lett. 40 (15), 3962–3967.

Portnov, A., Vadakkepuliyambatta, S., Mienert, J., Hubbard, A., 2016. Ice–sheet–driven methane storage and release in the Arctic. Nat. Commun. 7, 10314.

Prytherch, J., Yelland, M.J., 2021. Wind, convection and fetch dependence of gas transfer velocity in an Arctic sea–ice lead determined from eddy covariance CO_2 flux measurements. Global Biogeochem. Cycles 35 (2), e2020GB006633.

Prytherch, J., 2020. Wind and fetch dependence of gas transfer velocity in an Arctic sea-ice lead determined from eddy covariance CO_2 flux measurements. Earth Space Sci. Open Arch. https://doi.org/10.1002/essoar.10502449.1.

Prytherch, J., Brooks, I.M., Crill, P.M., Thornton, B.F., Salisbury, D.J., Tjernström, M., Humborg, C., 2017. Direct determination of the air–sea CO_2 gas transfer velocity in Arctic sea ice regions. Geophys. Res. Lett. 44 (8), 3770–3778.

Rampal, P., Weiss, J., Marsan, D., 2009. Positive trend in the mean speed and deformation rate of Arctic sea ice, 1979–2007. J. Geophys. Res.: Oceans 114 (C5), C05013.

Reeburgh, W.S., 2007. Oceanic methane biogeochemistry. Chem. Rev. 107 (2), 486–513.

Rösel, A., Itkin, P., King, J., Divine, D., Wang, C., Granskog, M.A., Gerland, S., 2018. Thin sea ice, thick snow, and widespread negative freeboard observed during N–ICE2015 north of Svalbard. J. Geophys. Res.: Oceans 123 (2), 1156–1176.

Shakhova, N., Semiletov, I., Salyuk, A., Yusupov, V., Kosmach, D., Gustafsson, Ö., 2010. Extensive methane venting to the atmosphere from sediments of the East siberian arctic shelf. Science 327 (5970), 1246–1250.

Shakhova, N., Semiletov, I., Sergienko, V., Lobkovsky, L., Yusupov, V., Salyuk, A., Nicolsky, D., 2015. The East Siberian Arctic Shelf: towards further assessment of permafrost–related methane fluxes and role of sea ice. Phil. Trans. Math. Phys. Eng. Sci. 373, 20140451, 2052.

Schuur, E.A., McGuire, A.D., Schädel, C., Grosse, G., Harden, J.W., Hayes, D.J., Vonk, J. E., 2015. Climate change and the permafrost carbon feedback. Nature 520 (7546), 171–179.

Silyakova, A., Jansson, P., Serov, P., Ferré, B., Pavlov, A.K., Hattermann, T., Niemann, H., 2020. Physical controls of dynamics of methane venting from a shallow seep area west of Svalbard. Continent. Shelf Res. 194, 104030.

Spreen, G., Kaleschke, L., Heygster, G., 2008. Sea ice remote sensing using AMSR–E 89–GHz channels. J. Geophys. Res.: Oceans 113 (C2).

Spreen, G., Kwok, R., Menemenlis, D., 2011. Trends in Arctic sea ice drift and role of wind forcing: 1992–2009. Geophys. Res. Lett. 38 (19).

Stroeve, J.C., Serreze, M.C., Holland, M.M., Kay, J.E., Malanik, J., Barrett, A.P., 2012. The Arctic's rapidly shrinking sea ice cover: a research synthesis. Climatic Change 110 (3–4), 1005–1027.

Thornton, B.F., Geibel, M.C., Crill, P.M., Humborg, C., Mörth, C.M., 2016. Methane fluxes from the sea to the atmosphere across the Siberian shelf seas. Geophys. Res. Lett. 43 (11), 5869–5877.

Thornton, B.F., Prytherch, J., Andersson, K., Brooks, I.M., Salisbury, D., Tjernström, M., Crill, P.M., 2020. Shipborne eddy covariance observations of methane fluxes constrain Arctic sea emissions. Sci. Adv. 6 (5), eaay7934.

Tohjima, Y., Zeng, J., Shirai, T., Niwa, Y., Ishidoya, S., Taketani, F., Sasano, D., Kosugi, N., Kameyama, S., Takashima, H., Nara, H., Morimoto, S., 2021. Estimation of CH_4 emissions from the East Siberian Arctic Shelf based on atmospheric observations aboard the R/V Mirai during fall cruises from 2012 to 2017. Polar Sci. 27, 100571 https://doi.org/10.1016/j.polar.2020.100571.

Upstill–Goddard, R.C., Rees, A.P., Owens, N.J.P., 1996. Simultaneous high–precision measurements of methane and nitrous oxide in water and seawater by single phase equilibration gas chromatography. Deep Sea Res. Oceanogr. Res. Pap. 43 (10), 1669–1682.

Vancoppenolle, M., Meiners, K.M., Michel, C., Bopp, L., Brabant, F., Carnat, G., Tison, J. L., 2013. Role of sea ice in global biogeochemical cycles: emerging views and challenges. Quat. Sci. Rev. 79, 207–230.

Verdugo, J., Damm, E., Nikolopoulos, A., 2021. Methane cycling within sea ice: results from drifting ice during late spring, north of Svalbard. Cryosphere 15, 2701–2717. https://doi.org/10.5194/tc-15-2701-2021, 2021.

Wanninkhof, R., 1992. Relationship between wind speed and gas exchange over the ocean. J. Geophys. Res.: Oceans 97 (C5), 7373–7382.

Wanninkhof, R., Asher, W.E., Ho, D.T., Sweeney, C., McGillis, W.R., 2009. Advances in quantifying air–sea gas exchange and environmental forcing. Ann. Rev. Mar. Sci 1, 213–244.

Wanninkhof, R., 2014. Relationship between wind speed and gas exchange over the ocean revisited. Limnol Oceanogr. Methods 12 (6), 351–362.

Weeks, W.F., Ackley, S.F., 1986. The growth, structure, and properties of sea ice. In: The Geophysics of Sea Ice. Springer, Boston, MA, pp. 9–164.

Westbrook, G.K., Thatcher, K.E., Rohling, E.J., Piotrowski, A.M., Pälike, H., Osborne, A. H., Hühnerbach, V., 2009. Escape of methane gas from the seabed along the West Spitsbergen continental margin. Geophys. Res. Lett. 36 (15), L15608.

Wiesenburg, D.A., Guinasso Jr., N.L., 1979. Equilibrium solubilities of methane, carbon monoxide, and hydrogen in water and sea water. J. Chem. Eng. Data 24 (4), 356–360.

Zhou, J., Delille, B., Eicken, H., Vancoppenolle, M., Brabant, F., Carnat, G., Geilfus, N.-X., Papakyriakou, T., Heinesch, B., Tison, J.-L., 2013. Physical and biogeochemical properties in landfast sea ice (Barrow, Alaska): insights on brine and gas dynamics across seasons. J. Geophys. Res.: Oceans 118 (6), 3172–3189.

Zhou, J., Tison, J.L., Carnat, G., Geilfus, N.X., Delille, B., 2014. Physical controls on the storage of methane in landfast sea ice. Cryosphere 8 (3), 1019–1029 (Data Availability Statement).